Received: 13 September 2020 | Revised: 13 March 2021 | Accepted: 18 March 2021

DOI: 10.1111/ijag.15920

INTERNATIONAL JOURNAL OF Applied Glass SCIENCE

ORIGINAL ARTICLE

Incorporation of calcium in glasses: A key to understand the vitrification of sewage sludge

Mariona Tarrago[1,2] | **Irene Royo**[1] | **Salvador Martínez**[1] | **Maite Garcia-Valles**[1] | **Daniel R. Neuville**[2]

[1]Department Mineralogia, Petrologia i Geologia Aplicada, Fac. de Ciències de la Terra. Universitat de Barcelona, Barcelona, Spain

[2]Université de Paris, Institut de Physique du Globe de Paris, CNRS, Paris, France

Correspondence
Mariona Tarrago, Department Mineralogia, Petrologia i Geologia Aplicada, Fac. de Ciències de la Terra. Universitat de Barcelona, c/ Martí i Franquès, s/n, Barcelona 08028, Spain.
Email: tarrago@ipgp.fr

Funding information
Consolidated Group for Structure and Materials Desing code, Grant/Award Number: 2017SGR1687; Fundació Bosch i Gimpera, Grant/Award Number: 307466; Ministerio de Educación, Cultura y Deporte, Grant/Award Number: FPU13/04507

Abstract

The quantity of sewage sludge generated daily by wastewater treatment plants represents a major environmental problem and a financial burden for plant operators. Valorization strategies focusing on reusing sewage sludge as a raw material are currently developed. Vitrification can help us reduce the volume of waste and binds the components in the structure of chemically stable glasses and glass-ceramics. In this study, the vitrification of sewage sludge inside a basaltic rock has been simulated by producing glasses and a glass-ceramic from basalt enriched in calcium that lie between the stability fields of pyroxene and melilite in the system $CaO–MgO–SiO_2–Al_2O_3$. CaO addition causes the oxidation of the melt at above the liquidus, increases the crystallization temperature, decreases the melting temperature, and improves the microhardness of the glasses. Glass-ceramic processes improves the properties of the Ca-doped basalt glass. The microhardness of the glass (8.2 GPa) and the glass-ceramic (8.6 GPa) and leaching tests (in the ppb range) place both the glass and the glass-ceramics at the high end of the mechanical properties and chemical resistance of ceramic tiles for the building industry.

KEYWORDS

basalt, crystallization, glass-ceramic, sewage sludg, viscosity

1 | INTRODUCTION

Each day, wastewater treatment plants generate huge volumes of waste in the form of sewage sludge, the solid fraction separated by the treatment (including domestic septage).[1] The disposal of sewage sludge is a worldwide issue: in 2010 the sum of wet sewage sludge produced in the United States, China and Europe reached 240 Mt; in 2017, global dry sewage sludge production rate was estimated at 45 Mt/year.[2] In Europe, 70% of the dry sewage sludge production—about 7 Mt/year—corresponds to Germany, the United Kingdom, Spain, Italy, and France. As a particular example, water processing in Catalonia (population 7.5 M) produced an average of 128,477 t/year of sewage sludge between 2004 and 2017.[3] The majority of this sludge is currently used as a substitute for fertilizers in agriculture (averaging 95,530 t/year), although 10 kt/year end up in landfills.

Environmental regulations are becoming increasingly restrictive in terms of usable sludge composition. Sewage sludge may contain potentially toxic elements (PTEs), such as Cr, Cu, Hg, or Pb, in concentrations that exceed those established by the European Economic Community for agricultural application by at least an order of magnitude.[4] The sources of PTE include domestic, agro-industrial and industrial wastewater, the corrosion of the sewerage system, and surface runoff from roads or urban areas.[5] Moreover, the excess sludge

unsuitable for agriculture is generally disposed of in landfills. This makes large areas become unsuitable for agriculture or any other economic activities and have associated economic costs that increase with the PTE concentrations.

Using sludge as a raw material would reduce the amount that needs to be disposed of. However, the large variability in the chemical compositions of sewage sludge requires a deep understanding of its effect on processing and the properties of the final products. The bulk composition of sewage sludge depends on the characteristics of its geographic source area. Indeed, factors such as urban/rural origin, processing methods at wastewater treatment plants, seasonal variations related to changes in upstream activity or in microbial activity,[6,7] long-term changes in soil uses of the watershed area, or the degree of groundwater contamination[8] control the variability and the chemical composition of sewage sludge. Such variability is problematic when producing materials with stable bulk compositions and which further retain any toxic elements contained in sludge.

In this study, we propose the use of basalt rock as an inertization matrix for sewage sludge. This mixture is interesting because the average composition of the inorganic fraction of urban sewage sludge (USS) is similar to that of the volcanic rock basalt (Table 1).[9] Furthermore, basalt is an inexpensive, commonly available volcanic rock that can be easily melted in industrial glass-making furnaces for the design and production of new glasses. Vitrified basalt is already used as abrasion-resistant tiles in walls or pavements by the building industry.[10] Using basalt glass to stabilize sludges will thus leverage an existing industry and help reducing the volume of the waste and binding of the components of the sludge—including the PTE—in the glass structure to retain any toxic elements, following a successful strategy employed for nuclear wastes.[11] Using basalt for the test also minimizes the concentrations of potentially toxic trace elements, which stay in all cases below 1 wt%.

To assess the viability of basalt glass as a remediation material for sludges, it is essential to understand how sludge assimilation will affect the glass long-term stability and how the elements are integrated in the glass structure. The main differences between basalt and sludge are the concentrations of Ca and P. CaO is sometimes used in the stabilization of P during wastewater treatment[50,51] and also to correct water hardness to make it suitable for drinking. The addition of P to basalt develops an increasingly sharp phosphate–silicate liquid–liquid phase separation in the glass above 4-wt% P_2O_5, the phosphate phase crystallizes during quenching above 16-wt% P_2O_5 and buffers the decrease of the microhardness of the final products.[52]

Further inertization can be achieved using a glass-ceramic process, where the PTE will be emplaced in newly-formed mineral phases.[53,54] The strengths of glass-ceramics as performing materials arise from their fine microstructure, achieved from the understanding of the nucleation and crystallization processes. Controlling the composition of the parent glass, the nucleation and crystallization processes, and their effect on the rheological behavior is also essential to achieve low viscosity at high temperature and to optimize the resistance to abrasion and chemical alteration.[53,54] Other interesting properties of glass-ceramics are their chemical stability, lack of porosity, and high strength and toughness.[55] Ca-rich wastes are good candidates for vitrification and subsequent glass-ceramic processing as seen in products such as Sital slag,[56] cupola slag blast,[57] blast furnace slag,[58] tin tailings,[59] molybdenum tailings,[60] and tungsten tailings.[61,62]

The objective of this study is to simulate the vitrification of a sewage sludge and basalt mixture using Ca-enriched basalts. We describe the glass-forming range, structure, thermal behavior, and crystallization and present the effect of chemical composition in microhardness and chemical durability. Additionally, we selected one composition to produce a glass-ceramic material and assess the effect of crystallization on its mechanical properties and chemical durability.

TABLE 1 Common chemical composition range of urban sewage sludge (USS),[10,12-47] mid-ocean ridge basalts (MORB),[48] and oceanic island basalts (OIB)[49]

Oxide (wt%)	USS	MORB	OIB
SiO_2	33-66	47-54	40-49
Al_2O_3	12-31	13-19	8-15
Na_2O	1-5	2-6	1-4
K_2O	1-7	0-3	0-6
CaO	8 -53	6-14	3-14
MgO	2-11	3-10	13-21
FeO	5-51	6-16	9-14
TiO_2	1-3	1-3	1-4
MnO	0-3	>1	>1
P_2O_5	3-33	0-1	>1

2 | MATERIAL AND METHODS

2.1 | Glass preparation and composition

Basalt–Ca glass batches with increasing concentration of CaO were prepared by mixing basalt from Boscarró old quarry[63,64] (Sant Joan les Fonts, SJLFB, Catalunya) with reagent grade $CaCO_3$ (Panreac 121212). The mixtures were homogenized by crushing in a ball mill and then melted in Al_2O_3 crucibles in a globular alumina furnace equipped with SuperKanthal® heating elements. The melting process consisted of heating the batch at 2°C/min up to 1000°C, followed by a 30-min isothermal step for decarbonation, and subsequently heating at 1°C/min up to 1450°C followed by a 4-h isothermal step. The melts were cast on a copper plate and a fraction was annealed in a TechnoPiro® muffle furnace preheated at 500°C for 24 hours. The samples are named as BXCa, where X is the percentage of added CaO.

The chemical compositions of the glasses were verified in a JEOL JXA 8230 electron microprobe (EMPA). The reported values correspond to the average of 10 measurements per glass composition. Quantitative electron microprobe analyses was obtained in wavelength-dispersive spectroscopy (WDS) mode, operating with an accelerating voltage of 20 kV, a beam current of 16 nA for Al, Si, Ti, Ca, K, Mg, Fe, Mn, 8 nA for Na and 6 nA for P, and a beam diameter of 5 μm. Corundum (Al$K\alpha$), wollastonite (Si$K\alpha$, Ca$K\alpha$), rutile (Ti$K\alpha$), orthoclase (K$K\alpha$), apatite (P$K\alpha$), periclase (Mg$K\alpha$), albite (Na$K\alpha$), synthetic Fe_2O_3 (Fe$K\alpha$), and rhodonite (Mn$K\alpha$) were used as standards. The analyzing crystals were TAP for Al and Si, PETJ for Ti, Ca, K and P, TAPH for Mg and Na and LIFH for Fe and Mn.

2.2 | Characterization

The density of the glasses was studied using the Archimedean method with toluene as immersion liquid. The mass of 10 glass fragments (weighing between 10 and 500 μg) per composition was measured in air (M_a) and immersed in toluene (M_t). The density of toluene (ρ_t) was corrected to account for the variation of temperature during the measurements using its equation of state[65,66]:

$$\rho_t = 0.8845 - 0.9159 \cdot 10^{-3}T + 0.368 \cdot 10^{-6}T^2 \quad (1)$$

The density ρ of the glasses was calculated using:

$$\rho = M_a \cdot \rho_t/(M_a - M_t) \quad (2)$$

The Raman spectra of the glasses were acquired using a T64000 Jobin–Yvon Raman spectrometer equipped with a CCD detector. The light source was an Ar^+ ion laser operating at a wavelength of 488 nm with a typical output of 100 mW on the sample. The spectra were acquired in a spectral range between 100 and 1500 cm^{-1} with an integration time of 600 s. The spectra were corrected using a cubic splines baseline and normalized to the total area.[65,67]

The thermal evolution of the glasses was studied by differential thermal analysis (DTA) in a Netzsch DTA-TG STA 409C equipment. Preliminary analysis was made on approximately 100-mg as-quenched glass powder (particle size <50 μm) at 10°C/min in an alumina crucible under 80 ml/min air flow and using pure Al_2O_3 (Perkin-Elmer 0419-0197) as a reference material. The equipment was calibrated using calcium oxalate, ensuring an error below 1°C.

The presence of amorphous and crystalline phases in the glasses and after thermal treatments was assessed on ground glass (grain size >45 μm) by X-ray diffraction (XRD) obtained in a PANalytical X'Pert PRO MPD Alpha1 powder diffractometer in Bragg-Brentano θ/2θ geometry (radius of 240 mm, Cu$K\alpha_1$ radiation (λ = 1.5406 Å), work power of 45 kV to 40 mA, scanning range 4-80° 2θ with step size of 0.017° and measuring time 50 s.

2.3 | Nucleation–crystallization experiments

The sample selected for the glass-ceramic study (as-quenched B16Ca) was then ground and screened to a particle size between 400 and 500 μm. These DTA measurements were done under 70 ml/min N_2 flow and using about 70 mg of glass sample in the aforementioned DTA-TG equipment. The glass particles were heated at 15°C/min up to treatment temperatures between 500°C and 850°C during 3 hours and then further heated up to 1350°C before cooling.

The effect of nucleation temperature (T_N) on bulk nucleation was evaluated using the shift of the crystallization peak temperature as described by Marotta and coworkers[68] for DTA runs carried out at constant heating rate and on samples of the same specific surface, held at different T_N for the same time. According to their method, the maximum of the curve representing the shift of the temperature of the exothermic peak as a function of the treatment temperature gives a curve that has the same shape and maximum as a curve representing the nucleation rate as a function of temperature.

Additionally, we performed instantaneous heating treatments to determine the nucleation sequence. About 30 mg of powdered B16Ca in Pt crucibles were introduced directly from room temperature into a SuperKanthal® furnace that was set at 600°C, 650°C, 700°C, 750°C, or 800°C and kept there for 6 hours. After this period, each batch was moved into another furnace that was set at the temperature of the exothermic peaks determined by DTA (856°C for the samples between 600-700°C and 870°C for the samples treated between 750°C and 800°C) in order to make the crystals grow without nucleating the intermediate phases. Finally, the samples were quenched to room temperature.

In situ XRD under vacuum atmosphere was carried out in an Anton Paar HTK1200 N High Temperature chamber (HT-XRD) coupled to the previously described equipment. The experiment consisted of heating powdered glass (grain size >45 μm) at a rate of 20°C/min with 1-h isothermal steps at 28, 300, 500, then from 550°C to 1200°C, and 28°C after cooling—7 spectra were taken during each one of these steps. Data from the HT-XRD patterns were used to determine how the intensity of certain peaks varies with temperature as well as to calculate the coherent size of the crystallites of each mineral phase nucleated during the thermal treatment from Scherrer's equation[69]:

$$\tau = \frac{K\lambda}{\beta\cos\theta} \quad (3)$$

In this equation, τ stands for the average size of the crystalline domains; K is a dimensionless shape (0.9), λ is the X-ray wavelength (1.5406); β is the full width of the peak at half maximum minus the instrumental line broadening, in radians; and θ is the Bragg angle—in radians. The quantification of the mineral phases of the glass-ceramic was obtained from the Rietveld refinement of the XRD nonoriented powder diffraction on FullProf v 3.00 software.[70]

The dependence of viscosity on temperature was determined using a hot-stage microscopy (HSM) prototype.[71] The test cylinders were made in a uniaxial press by compressing about 40 mg of glass powder (diameter <45 μm) bound with a 1/20 solution of Elvacite® in acetone. The sample was heated at 5°C/min between 25°C and 1450°C. The deformation was recorded using the ProgRes CapturePro 2.8.8. software. The images corresponding to the fixed viscosity points were identified using Hot-Stage software.[71] The viscosity–temperature curves were plotted using the temperatures of the fixed viscosity points determined during the HSM analysis and the viscosity values from Pascual and coworkers.[72]

The Vickers hardness (VH) of the samples was measured on polished glass probes using a Galileo Isoscan OD Vickers microindenter with a load of 2.94 N. Each value corresponds to the average of 10 measurements. The experimental error was 0.3 GPa.

2.4 | Glass-ceramic preparation and characterization

The thermal treatment of a bulk fragment (weight about 2 g) of the parent glass of composition B16Ca to obtain the glass-ceramic included the following steps based on the crystallization sequence determined during the study:

- Heating up to 650°C at 2°C/min for 6 hours (T_N of magnetite)
- Heating at 675°C at 2°C/min for 6 hours (second T_N, discussed further in the manuscript)
- Heating up to 874°C at 10°C/min for 6 hours (the temperature of the exothermic DTA peak)
- Heating to 1000°C at 2°C/min for 6 hours (at this temperature merwinite has been exhausted by reacting with diopside to form akermanite)
- Free cooling

Texture was observed in a JEOL J-7100 field emission scanning electron microscope (SEM) with EDS detector and backscattered electron detector (BDS). The redox ratio (Fe^{3+}/Fe_{tot}) was calculated using the model by Kress and Carmichael.[73]

The chemical durability of the glasses and the glass-ceramic was evaluated according to the procedure specified in DIN 38414-S4.[74] The tests were performed on 10 g of samples B16Ca and its corresponding glass-ceramic GC-B16Ca, using a particle fraction between 2 and 4 mm—dried at 50°C and mixed in 100 ml of deionized water. The mixture was agitated at room temperature during 24 hours, and the liquid was separated from the solid using a 0.45-μm pore size filter. The leachates were analyzed by inductively coupled plasma optical emission spectrometry (ICP-OES, Optima 3100×, PerkinElmer) and inductively coupled plasma mass spectrometry (ICP-MS, Elan 6000, PerkinElmer).

3 | RESULTS

3.1 | Glass characterization

The chemical composition of the studied glasses consists of a set of Ca–basalt mixtures with increasing Ca content covering the compositional gap between USS and basalts (Table 2). There is some contamination of the glasses with Al_2O_3 due to the reaction with the crucibles used to melt the Ca–basalt mixtures. However, it is smaller than the increase in CaO, which is assumed to remain the main driving factor of the changes in structure and macroscopic properties. The limit of Ca concentration was established at 32 mol%, as sample B32Ca partially crystallized into merwinite during casting at higher CaO concentrations.

The density of the glasses increases with Ca addition because the molecular weight of CaO is higher than the average molecular weight of the basalt (Figure 1). M/A (where M = CaO + MgO + Na_2O + K_2O and A Al_2O_3 in % mol, Table 2) increases with added CaO.

The Raman spectra of the glasses (Figure 2) may be divided in three broad regions. The low frequency envelope (LF) is located between 250 and 630 cm^{-1}, the middle frequency envelope (MF) between 630 and 785 cm^{-1}, and the high frequency envelope (HF) between 785 and 1250 cm^{-1} (Figure 2). The LF envelope, linked to vibrations of bridging oxygen along T-O-T bonds,[67,75-82] becomes more localized with Ca addition. A band rises at 300 cm^{-1} with increasing Ca addition. These low frequency vibrations are linked to the bending vibrations of the network-modifying cations.[83] The MF corresponds to the intertetrahedral bending mode of polymerized species.[84,85] At low Ca contents, it forms a shoulder of the LF; the vibration becomes more localized with increasing Ca. The HF envelope is attributed to the vibrations of $T\text{-}O^-$ bonds—where T stands for the fourfold coordinated cations Si^{4+}, Al^{3+}, Fe^{3+}, and O^- for bridging or nonbridging oxygen (BO and NBO)—and the structural effect of network-modifying and charge-balancing cations (see previous studies[67,78,79,85-89]). Overall, the envelope shifts to higher frequencies with Ca addition (see the higher limit of the HF around 1100 cm^{-1}). The intensity of the envelope increases

TABLE 2 Chemical composition of the Ca-doped glasses expressed in wt% and mol%, and M/A

wt% *mol%*	SiO_2	Al_2O_3	CaO	MgO	Na_2O	K_2O	MnO	FeO	TiO_2	P_2O_5	M/A
B0	43.9 (4)	18 (1)	9.2 (2)	9.9 (3)	3.0 (1)	1.53 (3)	0.19 (3)	11.2 (3)	2.5 (4)	0.6 (1)	
	46.4	*11.2*	*10.4*	*16.5*	*3.1*	*1.0*	*0.2*	*9.9*	*2.0*	*0.3*	*2.7*
B2Ca	42.7 (3)	13.8 (1)	11.7 (2)	10.5 (2)	3.4 (1)	1.6 (1)	0.19 (3)	11.5 (1)	2.4 (1)	0.5 (1)	
	44.9	*8.5*	*13.2*	*16.5*	*3.5*	*1.1*	*0.2*	*10.1*	*1.9*	*0.2*	*4.0*
B4Ca	41.7 (3)	14.0 (6)	13.4 (2)	10.2 (4)	3.1 (2)	1.44 (7)	0.18 (3)	11.2 (3)	2.4 (1)	0.5 (1)	
	43.9	*8.7*	*15.1*	*16.0*	*3.2*	*1.0*	*0.2*	*9.9*	*1.9*	*0.2*	*4.1*
B8Ca	40.0 (3)	13 (1)	16.5 (3)	9.9 (6)	3.1 (1)	1.49 (7)	0.18 (3)	10.7 (3)	2.28 (8)	0.5 (1)	
	42.1	*8.1*	*18.6*	*15.5*	*3.2*	*1.0*	*0.2*	*9.4*	*1.8*	*0.2*	*4.8*
B16Ca	36.1 (3)	12.2 (2)	24.4 (3)	9.2 (6)	2.3 (1)	1.12 (7)	0.15 (3)	10.1 (3)	2.0 (1)	0.5 (1)	
	37.5	*7.5*	*27.1*	*14.2*	*2.3*	*0.7*	*0.1*	*8.8*	*1.6*	*0.2*	*6.0*
B24Ca	32.7 (4)	14 (1)	28.8 (5)	8.0 (2)	2.4 (1)	1.1 (1)	0.13 (3)	8.6 (2)	1.8 (1)	0.4 (1)	
	34.2	*8.6*	*32.3*	*12.5*	*2.4*	*0.7*	*0.1*	*7.5*	*1.4*	*0.2*	*5.6*
B32Ca	29.5 (4)	10.0 (5)	36.6 (6)	7.9 (3)	2.0 (1)	0.84 (5)	0.15 (3)	8.3 (2)	1.70 (8)	0.4 (4)	
	30.3	*6.1*	*40.3*	*12.1*	*2.0*	*0.6*	*0.1*	*7.1*	*1.3*	*0.2*	*9.1*

Note: The error of the EMPA analyses (in wt%) is represented by the standard deviation of the measurements.

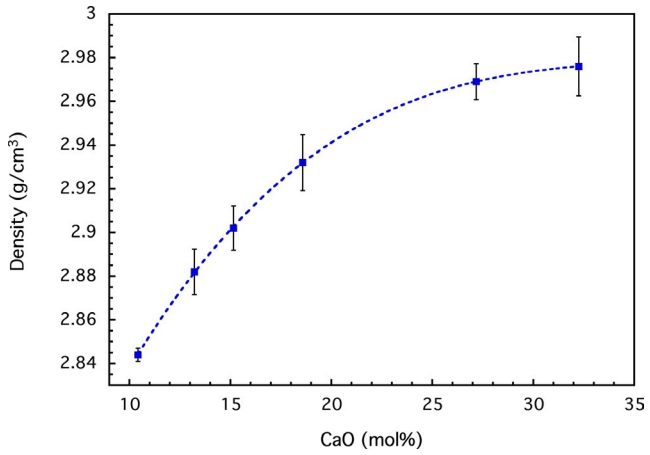

FIGURE 1 Density of the glasses as a function of CaO contents. The dashed line is a guide for the eye. The error represents the 1σ standard deviation of the measurements

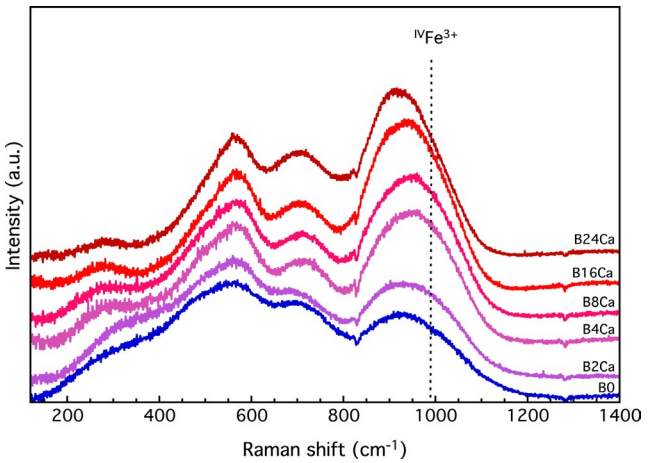

FIGURE 2 Raman spectra of the glasses. The line at 990 cm^{-1} shows the position of the stretching vibration of $^{IV}Fe^{3+}$–O bonds. The bumps near 830 and 1275 cm^{-1} are glitches from the CCD detector

with the growth of a localized contribution around 990 cm^{-1} that shifts to lower frequencies with increasing CaO. This band is linked to the stretching vibration of fourfold coordinated Fe^{3+}–O bonds and its intensity increases when the melt becomes more oxidized and enriched in Fe^{3+}.[90-94] The presence of this strong vibration in our glasses is in very good agreement with the redox calculated using different models.[73,95]

The thermal behavior of the Ca-doped basalt glasses shows the glass transition and three main exothermal events linked to the formation of different crystalline phases (Figure 3). The endothermic events around 660-710°C correspond to the glass transition. The first exothermic signal is a peak that shifts from 739°C to 819°C with Ca addition. The second signal is a sharp peak at 855°C that becomes larger and shifts up to 894°C with increasing Ca contents. A shoulder grows at 870°C on sample B16Ca, whereas the peak is much broader for sample B24Ca. The endothermic events above 1100°C correspond to the melting of the system, which increases with added Ca as the bulk composition shifts from the pyroxene to the melilite stability field.[96]

The crystallization process evolves with increasing Ca contents (Figure 4). The main exothermal event at about 850°C corresponds to the crystallization of an assemblage

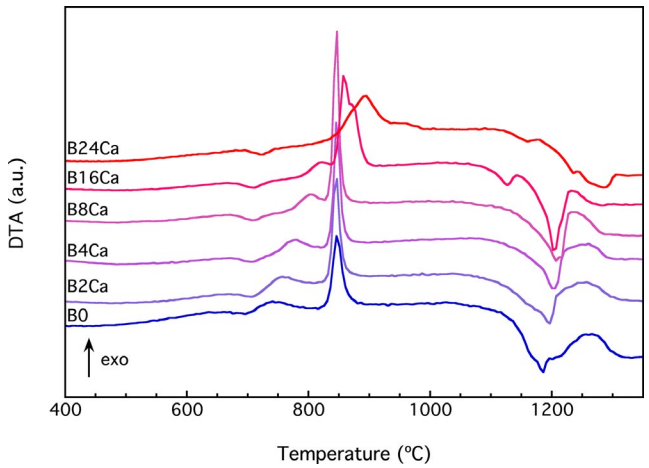

FIGURE 3 DTA curves of the glasses measured at 10°C/min

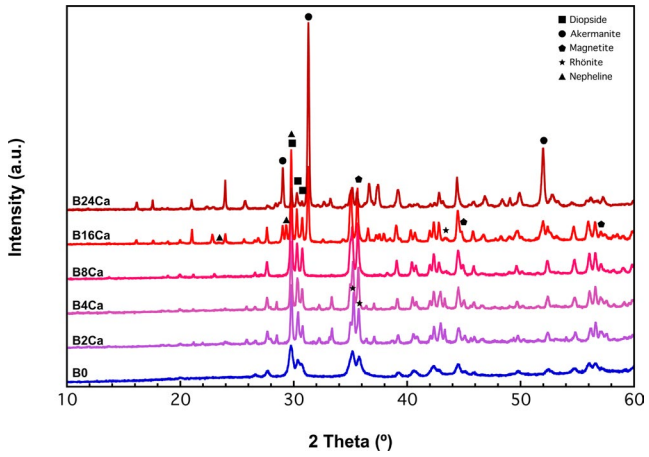

FIGURE 4 Diffractograms of the glasses treated at the temperature of the main exothermic peak measured using DTA. The labels correspond to the three main diffraction peaks of each phase

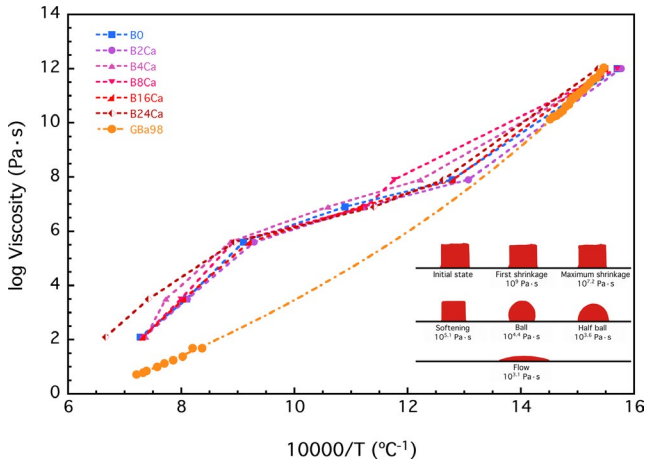

FIGURE 5 Evolution of the viscosity with Ca addition. The data from this study correspond to glasses that crystallize during the experiments. The GBa98 data were obtained from creep and rotational viscometry measurements on crystal-free melts.[91] Errors are smaller than symbol sizes. Curves are guides for the eye. The inset presents the images corresponding to the fixed viscosity points for the measurement on sample B16Ca after the processing using Hot-Stage software[71]

of magnetite (Fe_3O_4) and diopside ($CaMgSi_2O_6$) for all the samples. Rhönite ($(Ca_2(Mg^{2+}Fe^{2+}Fe^{3+}Ti^{4+})_6(Si, Al)_6O_{20})$ is detected between 10.4- and 18.6-mol% CaO. It is a 4-chained inosilicate that may be a precursor of diopside and small amounts of it remain at low CaO concentrations. Akermanite and nepheline crystallize starting at 27.1-mol% CaO as the composition lies on the limit between the pyroxene and the melilite stability field. The abundance of pyroxene decreases in favor of akermanite with further increase of the Ca concentration. Overall, the crystalline assemblages are in good agreement with the location of the samples in the CMAS phase diagram.[97]

Designing an appropriate production process requires knowledge of the viscosity of the melt during glassmaking. The evolution of viscosity as a function of Ca addition is complex (Figure 5). The curves of the Ca-doped glasses are compared to a natural basalt (GBa98) from Piton de la Fournaise volcano.[98] The viscosity of GBa98—measured by creep and rotational viscometry—decreases steadily over the whole range, faster at low temperatures, and slower at higher temperatures. The viscosity curves of the Ca-doped basalt glasses first decrease steadily with increasing temperature and form a convex shape afterwards, where viscosity is reduced slower than expected; the shape of the tested cylinders undergoes all the shapes correlated to the fixed viscosity points of HSM experiments (see inset in Figure 5). This effect is caused by the crystallization observed on DTA between 850°C and 900°C. In viscous melts, the formation of crystals increases the viscosity by hampering the movement of the liquid phase. The variation of viscosity with Ca addition is influenced by two conflicting processes: the depolymerization related to the increase of Ca that reduces viscosity, and the formation of $^{IV}Fe^{3+}$–O bonds and crystallization that increase it. Hence, the results represent the apparent viscosity of the glass–crystals mixtures. The oxidation of Fe as a consequence of Ca addition causes a large increase in viscosity in the high temperature range—as observed in sample B24Ca below 104 Pa·s—which is also consistent with the increase of the melting point of the system observed in DTA. B16Ca has the lowest melting temperature of the system, in agreement with its location on the boundary of the stability fields between two phases.

The Vickers microhardness of the Ca-doped basalt glasses is between 7.0 and 8.6 GPa and generally rises with increasing Ca (Figure 6). The initial decrease (although it must be noted it is barely on the error range) could be linked to the

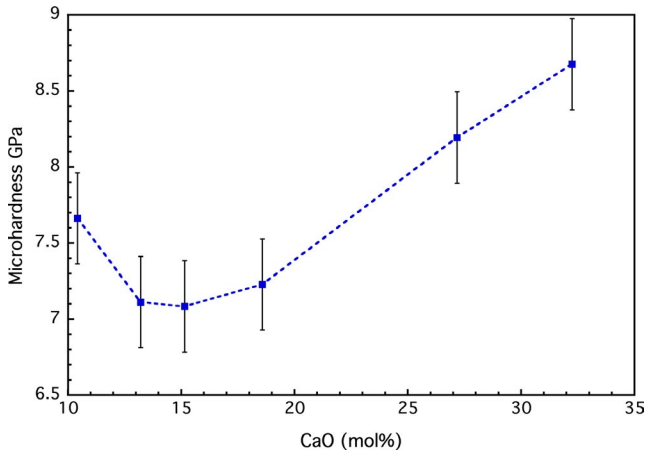

FIGURE 6 Vickers microhardness of the Ca-doped basalt glasses. Errors are given at the 1σ confidence interval. The curve is only a guide for the eyes

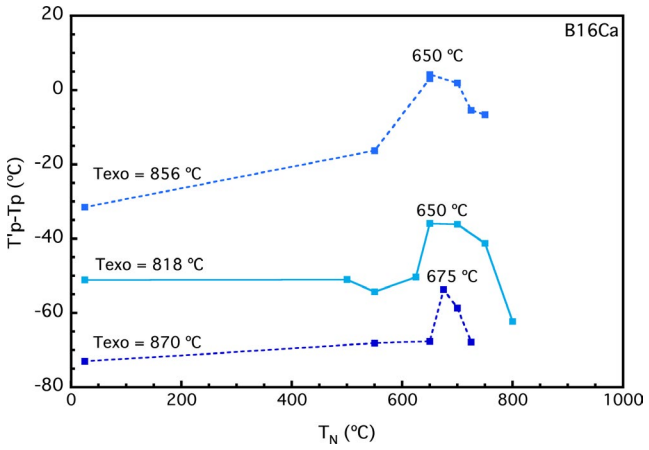

FIGURE 7 Shift of the temperature of the exothermic peak as a function of the nucleation temperature corresponding to the three exothermic events for sample B16Ca. Lines are guides for the eyes. Errors are smaller than symbol sizes

excess Al_2O_3 coming from the melting crucible. Afterwards, the microhardness is increased as the structure becomes more compact due to the addition of network modifiers, similar to the rise in density. The microhardness of P-bearing, Ca-doped basaltic glasses increases in a similar manner.[99] The addition of network modifiers has been proved to improve the mechanical properties of basalt fibers.[100]

We selected sample B16Ca (27.1-mol% CaO) to develop a glass-ceramic because it contains the highest amount of Ca without increasing viscosity at high temperature. The flow point, corresponding to a viscosity of $10^{2.1}$ Pa·s, is reached at 1365°C instead of 1501°C for sample B24Ca. Its microhardness is also the second highest one in the whole set. All further experiments have only been performed on sample B16Ca.

3.2 | Determination of the temperatures of maximum nucleation rate and crystal growth

The treatment temperatures (T_T) for sample B16CCa are obtained from the shift of the exothermic peak corresponding to crystallization measured on glass treated at different nucleation temperatures (T_N). T'p–Tp is the difference between the temperature of the DTA exothermic peak of the as-quenched glass (T'p) and the DTA exothermic peak of the nucleated glass. Plotting T'p–Tp as a function of T_N results in a curve whose maximum is located at the same value as T_N determined by classical methods.[68] This approach should supply T_N for each of the mineral phases that crystallize from a parental glass. Two different events have been isolated. The first is a broad peak centered at 650°C from the shift of both the exothermic peaks at 818°C and 856°C (Figure 7), which appear in all the analyses. The second is a narrower peak centered at 675°C, which is only detected for T_N below 750°C, corresponding to the variation of the shoulder at 870°C (Figure 7).

The crystallization sequence and a tentative attribution of the T_N are determined from the evolution of the intensity of the main diffraction peak after instantaneous heating from room temperature to T_N and further heating up to the temperature of the exothermic event (T_{exo}) from DTA to induce crystal growth (Table 3 and Figure 8). Each of these treatments is noted as $T_N(+T_{exo})$.

Magnetite (Fe_3O_4) is the only phase that crystallized during the treatment at 600(+856)°C and the most intense at 650(+856)°C (Figure 8A and Table 3). Hence, it is the most likely phase to have nucleated in the first event at 650°C. The sequence continues with the simultaneous crystallization of nepheline ($Na_3\ K(Si_{0.56}Al_{0.44})_8O_{16}$) and diopside ($Mg_{0.6}Fe_{0.2}Al_{0.2}Ca(Si_{1.5}Al_{0.5})O_6$). Both have crystallized for the first time on the sample treated at 650(+856)°C. Merwinite ($Ca_3MgSi_2O_8$) appears at 700(+856)°C. The proximity and overlap between all these events makes it difficult to attribute the second event at 675°C to the nucleation of a single phase with the available data (Figure 8). Akermanite ($Ca_2(Mg_{0.75}Al_{0.25})[Si_{1.75}Al_{0.25}O_7]$,) is detected starting at 750(+856)°C.

3.3 | Evolution of the crystalline phases in the devitrification process

In situ XRD patterns show the crystallization of newly-formed mineral phases in sample B16Ca between 770°C and 1200°C (Figure 9A) and the appearance of the first crystals (Figure 9B). The glass stays amorphous up to 760°C and the first diffraction peaks can be detected at 770°C.

TABLE 3 Intensities of the main diffraction peaks of the newly-formed mineral phases after instantaneous thermal treatments of sample B16Ca at the T_N followed by growth at the temperature of the first exothermic

	Newly-formed minerals (cps)				
T_N (°C)	Magnetite 01-088-0315[101]	Nepheline 01-076-2467[102]	Diopside 01-072-1379[103]	Merwinite 01-089-2432[104]	Akermanite 01-079-2424[105]
600	113	—	—	—	—
650	301	63	431	—	—
700	165	167	265	—	—
750	—	1726	6001	2697	33
800	—	1450	5892	2218	1893

Note: The numbers correspond to the powder diffraction file (PDF) used for the identification in bold.

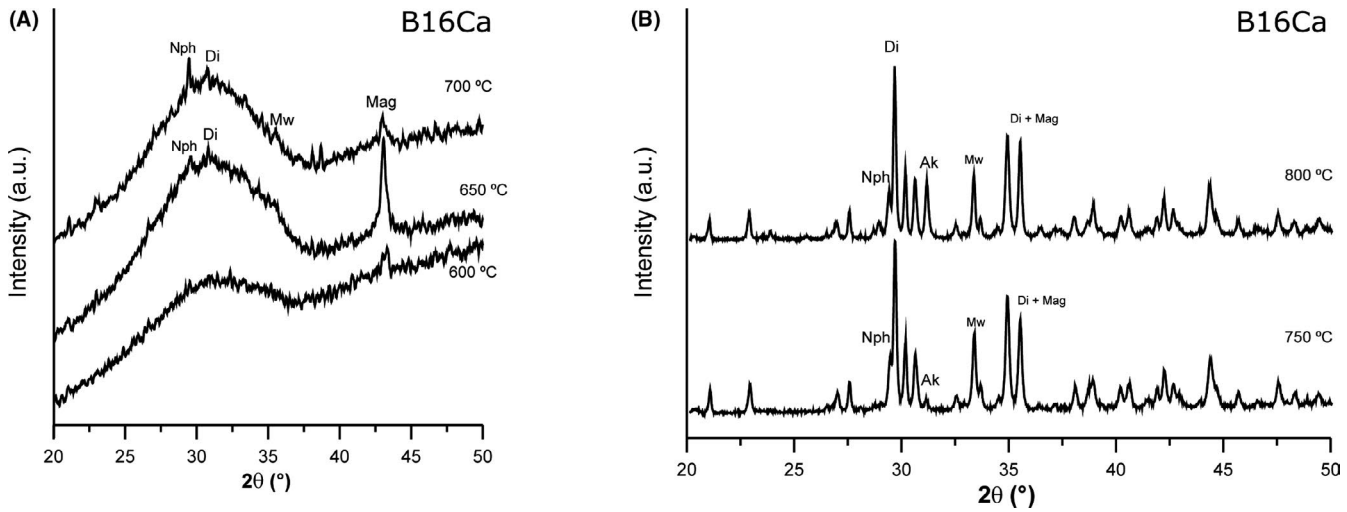

FIGURE 8 Sequence of XRD patterns obtained after instantaneous heating of sample B16Ca at (A) 600-700°C and (B) 750-800°C for each phase. The temperatures in the plot correspond to the T_N of each treatment

Diopside, nepheline and merwinite can be seen in the HT-XRD pattern at 770°C, whereas akermanite is detected from 800°C (Figure 9A). The evolution of the intensity of each of the mineral phases has been tracked using the following diffraction peaks: d_{201} for nepheline, d_{310} for merwinite, d_{310} for diopside, and d_{211} for akermanite (Figure 10). They are the most intense that did not overlap with peaks from coexistent phases. The evolution of magnetite could not be tracked in this experiment because its main diffraction peak overlaps with a major peak of diopside and the rest of reflections are not intense enough.

Nepheline is stable between 760°C and 1080°C, with maximum intensity at 860°C. Merwinite has a similar behavior: it also reaches a maximum at 860°C and becomes undetectable over 980°C. The peak intensities of akermanite increases during the decrease of these two phases, reaches its maximum at 970°C, and becomes undetectable at 1190°C. The peak intensity of diopside increases along the whole temperature range, alongside with the crystallization and melting reactions of merwinite and akermanite (Figures 9 and 10). The sample does not undergo additional changes during cooling.

The sizes of coherent crystals at each temperature are calculated using Scherrer's equation to establish the growth of each phase. The maximum crystal size reached in HT-XRD for all the minerals is between 40 and 70 nm. This can be due to the fact that all phases nucleate in a narrow temperature range, hence forming a large number of nuclei before reaching the crystal growth temperature (T_{GR}) and constraining crystal growth. Magnetite crystals are still smaller, reaching a maximum of 18 nm. Their role is to act as a nucleus for the growth of diopside, and they are absorbed inside its structure to approach the Fe-rich end-member.

3.4 | Glass-ceramic characterization

The glass-ceramic has been obtained through the thermal treatment of the parent glass based on the T_N and T_{GR} exposed earlier. It is formed by nepheline (12.15 wt%), magnetite (6.03 wt%), diopside (41.32 wt%), and akermanite (40.50 wt%) (Figure 11).

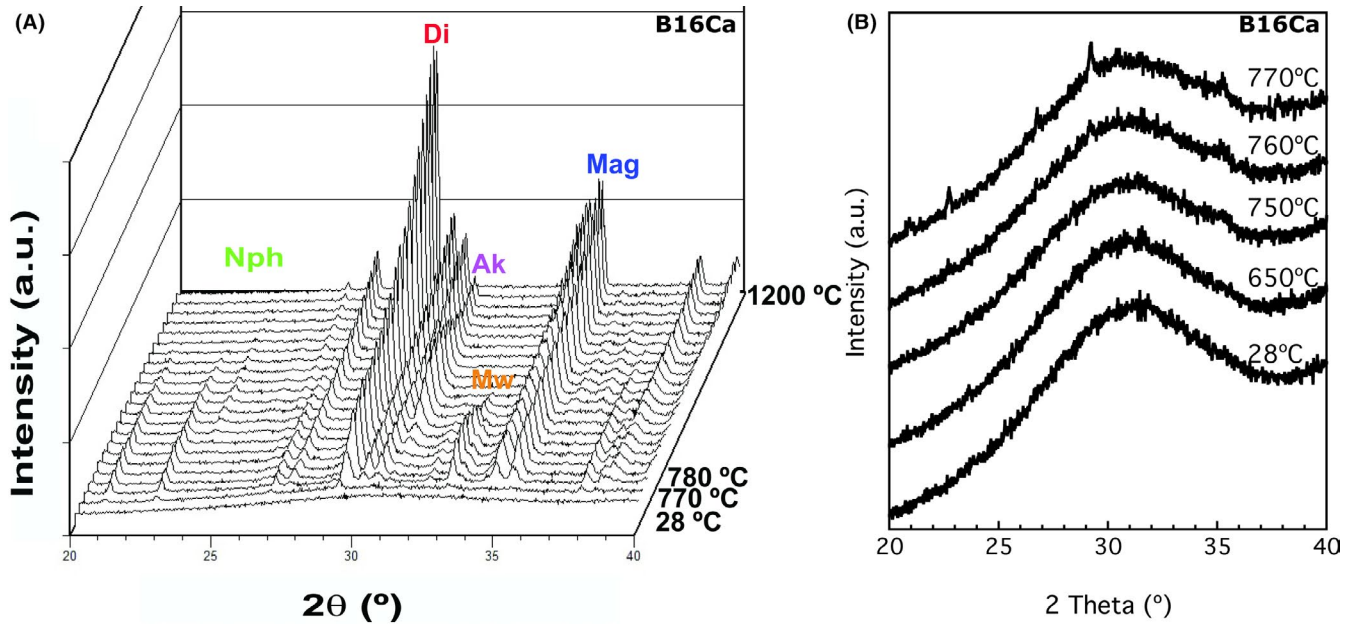

FIGURE 9 (A) HT-XRD patterns of thermally treated B16Ca for 2θ between 20° and 40°. The first pattern is recorded at room temperature. The labels represent the peak chosen to study the evolution of each phase with temperature. (B) Patterns measured between room temperature and 770°C, showing that the first crystals appear at 770°C

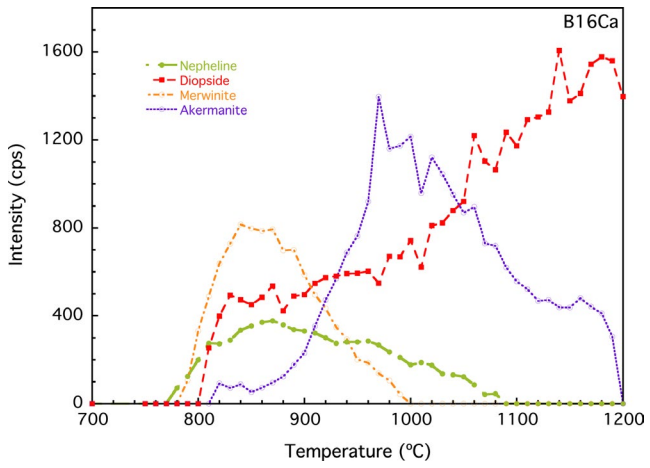

FIGURE 10 Evolution of the intensities of selected XRD peaks of thermally treated B16Ca (d_{201} for nepheline, $d_{310}$for merwinite, d_{310} for diopside, and d_{211} for akermanite) as a function of temperature

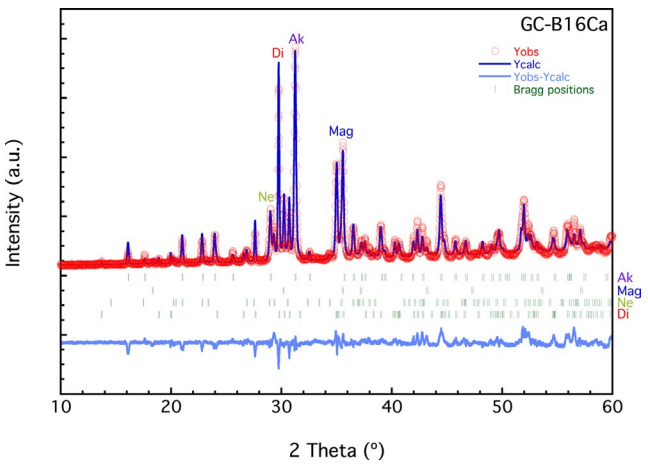

FIGURE 11 Refined XRD pattern of the glass-ceramic based on sample B16Ca showing the observed intensity (Yobs) of the experiment, the calculated intensity of the Rietveld refinement (Ycalc), the difference curve and the Bragg positions of the diffraction for each mineral phase. The labels identify the maximum intensity diffraction peak of each crystalline phase

Treating the parent glass at the T_T generates a large number of nuclei, which grow upon further heating and result in a fine-grained glass-ceramic. The bulk microstructure of the glass-ceramic observed on SEM consists on idiomorphic crystals ranging between 60 and 120 nm (Figure 12). Diopside, akermanite, and nepheline form a homogeneous grain microstructure. The observed sizes of the crystals are larger than 40-70 nm obtained from Scherrer's equation for diopside, nepheline, and akermanite and 18 nm for magnetite. This difference is due to the longer crystallization steps used in glass-ceramic production compared to those for in situ HT-XRD.

The Vickers microindentation test has given a microhardness of 8.2 GPa (Figure 6) for the parent glass and of 8.6 GPa for the glass-ceramic. These values lie in the hardness range of the diopside–hedenbergite series (from 7.7 to 9.8 GPa), are higher than the augite series (from 6.6 to 8.0), and are considerably higher than the hardness of akermanite (5.2-6.6 GPa). The abundance of diopside is the main contributor to the increase of the microhardness,

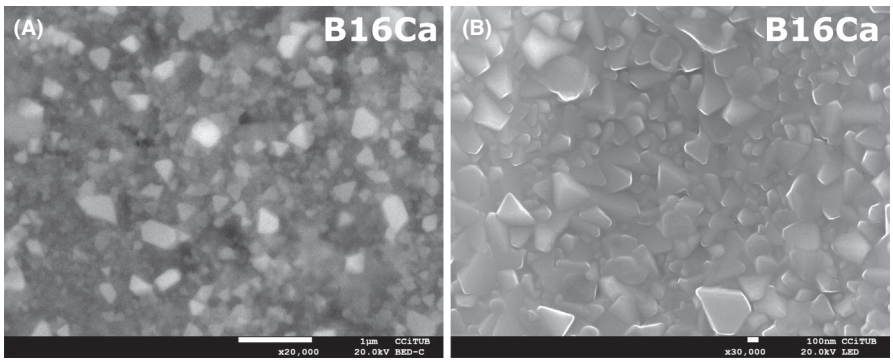

FIGURE 12 SEM micrographs showing the texture of the glass-ceramic. (A) a BDS image of the mass of the crystals where dense magnetite crystals stand out (B) a detail of the mixture of fine grained idiomorphic diopside, akermanite and nepheline

TABLE 4 Concentration of selected elements on the leachates recovered from the chemical durability tests of samples B16Ca (glass) and GC-B16Ca (glass-ceramic) of after blank subtraction

[ppm] in solution	Si	Al	Na	K	Ca	Mg	Fe	Ti	P
B16Ca (glass)	4.17	1.18	9.73	2.24	3.52	2.73	0.39	$76.32*10^{-3}$	BB
GC-B16Ca (glass-ceramic)	4.79	0.88	8.31	1.88	4.43	2.45	0.11	$26.73*10^{-3}$	BB

Note: BB stands for "below blank concentration."

which leads to an improvement on the mechanical properties of the obtained material.

The glass-ceramic process has increased the overall stability of the glass, as the concentration of most of the elements in the glass-ceramic leachate is lower than in the glass leachate (Table 4). However, the leachability of Ca and Si is higher from the glass-ceramic than the glass. The concentration of each element in the leachates is several orders of magnitude below their concentrations in the original basalts.

4 | DISCUSSION

The composition of the parent glass B16Ca corresponds to the border between the stability fields of pyroxene and melilite in the section at 10-wt% Al_2O_3 of the phase diagram of the system $CaO–Al_2O_3–MgO–SiO_2$, the major glass components. The crystallization of akermanite—the magnesian end-member of the melilite solid solution ((Ca, Na)(Al, Mg, Fe^{2+})[(Al, Si)SiO_7])—and its relationship with merwinite is a controversial question in the literature.[58] Merwinite is often a found as a metastable phase formed during the thermal treatments of multicomponent glasses in the initial stages of the devitrification process, around T_g. The relaxation of the glass structure at higher temperatures will facilitate the diffusion of ions[43] causing the destabilization of merwinite, which will react with the other minerals to produce the stable mineral phases according to the phase diagram of the system.[97]

A study of the crystallization of a glass of a composition in the akermanite–gehlenite system ($2CaO·(1 - x)·MgO·x-Al_2O_3·(2 - x)SiO_2$) proved that merwinite is a metastable phase for all x below or equal to 0.6 and attributed this fact to structural reasons.[106] In the case of the melilite minerals, corresponding to the sorosilicate group, the structure consists in a fragmented network of silica tetrahedra, and modifier cations are stabilized by the ionic bonds between the tetrahedra and the cations.[58] Merwinite is a nesosilicate and thus presents a lower concentration of silica tetrahedra, creating a less strong network that melts at lower temperature.[106] The formation of akermanite may then be explained from the diffusion of calcium from merwinite to diopside described by the reaction merwinite + diopside = akermanite:

$$3CaO \cdot MgO \cdot 2SiO_2 + CaO \cdot (MgO, FeO) \cdot 2SiO_2 = 2CaO \cdot (MgO, FeO) \cdot 2SiO_2 \quad (4)$$

The bulk composition of the parent glass can be expressed as $2CaO·1.05MgO·0.55Al_2O_3·2.76SiO_2$ using the formula of melilite. In this case, x (the number of moles of Al_2O_3) is effectively below 0.6, and then merwinite is metastable. Moreover, the already insufficient concentration of Al in the system is also influenced by the formation of nepheline during the devitrification process. Nepheline is the phase with a higher Al concentration between those formed during the devitrification process; its formation extracts Al from the system, destabilizing merwinite and enhancing the crystallization of akermanite. Even the melting of nepheline over 860°C does not reintroduce enough Al in the system to allow the formation of merwinite, and thus it is absent from the glass-ceramic.

The production process of GC-B16Ca has provided a crystalline material with a fine microstructure. The thermal treatment of the glass to the nucleation temperature for an extended period (in this case, 6 hours) followed by heating of the sample up to the growth temperature enabled us to minimize the presence of metastable phases such as merwinite. Obtaining extensive nucleation on a glass-ceramic based on basalt requires a Fe_2O_3/FeO ratio of at least 0.5.[107] The

raw basalt Fe_2O_3/FeO equals 0.501,[108] and supplementary oxidation is provided by melting the ground basalt under air atmosphere.[55] In the BXCa series (the pristine glasses), Fe^{3+}/Fe_t, calculated using the model by Kress and Carmichael[73] increases from 0.42 to 0.65 with the addition of CaO (Figure 13). The addition of Ca pushes Fe to oxidize and take a network forming role, which in its turn increases the glass transition temperature. The significant concentration of FeO (7.5 mol%) and TiO_2 (1.4 mol%) favors bulk nucleation.

The microhardness of the glass and the glass-ceramic lies on the same range, and near the higher limit, of the reported values for basalt glasses and glass-ceramics in the literature (Table 5). The extensive nucleation of the parent glass creates a fine microstructure and limits the eventual formation of porosity due to crystal growth, making the glass-ceramic harder than the glass in spite of bearing approximately 40 wt% of akermanite (5.2-6.6 GPa). The trend of increasing hardness is a promising advocate for the glass-ceramic process as a means for improving the mechanical properties of multicomponent glass.

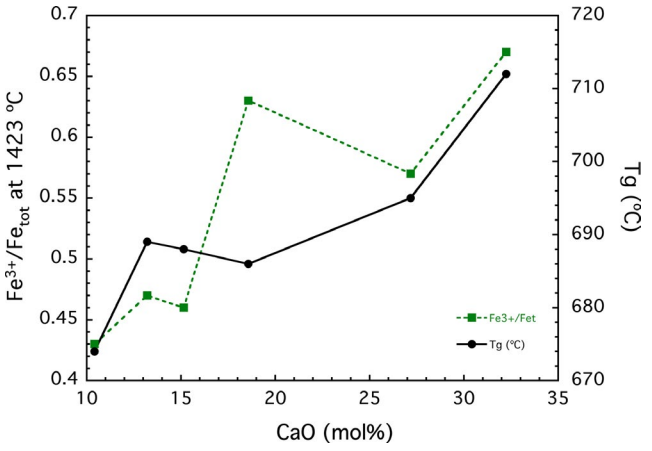

FIGURE 13 Redox of the melt at 1423°C calculated using the model by Kress and Carmichael[73] and glass transition temperature measured by DTA

TABLE 5 Microhardness results of this study compared to Vickers microhardness values for basaltic glasses and glass-ceramics[109-111]

Material	Vickers microhardness (GPa)
Glasses of this study	7.1-8.7
B16Ca glass	8.2
B16Ca glass-ceramic	8.6
Canary Island Basalt glass[109]	5.2-6.3
Canary Island Basalt glass-ceramic[109]	6.6-8.7
Basalt rock fiber glass[110]	7.7
Basalt glass/crystal mixtures[110]	6.8-8.9
Holyoke basalt glass[111]	8.9

Glass-ceramics are generally characterized by a good chemical resistance, comparable to other ceramic materials.[112] In this study, the leachability tests provided complex results. The decrease in the concentrations of most of the main components between the leachates of the glass and the glass-ceramic points to an overall better inertization potential. However, the leachability of Ca and Si is lower in the glass than in the glass-ceramic. Fredericci and coworkers[58] observed a similar situation in the increase of weight loss between a blast furnace slag glass and glass-ceramics. This situation might be caused by the high amount of akermanite, which is the phase with higher Ca and Si contents of the glass-ceramic.

Basaltic glasses are already in use as pavements in intensive-use industrial facilities[10] or in public transportation such as in Barcelona's subway station Rocafort. Hence, a product such as B16Ca or GC-B16Ca could find a use that enabled the recycling of sewage sludge. The presence of magnetite and diopside in the mineralogy of the glass-ceramic shows a good potential for the inertization of PTE usually present in sludge such as Cr or Zn[12,23,34] because they could be hosted in the spinel structure or in the pyroxene lattice.

5 | CONCLUSIONS

We achieved the vitrification of a set of Ca–basalt mixtures analogous to sewage sludge. The addition of up to 17-mol% CaO—total concentration of 27 mol%—contracts and polymerizes the network due to the oxidation of Fe, which takes a network-forming role. The density and the microhardness of the samples also increase with CaO addition; its viscosity at high temperature does not change significantly up to 27.1-mol% CaO. We produced the glass-ceramic of the composition containing 27-mol% CaO based on the determination of the temperatures of maximum nucleation rate and crystal growth of the newly-formed phases. The result is a nanometric homogeneous microstructure which improved the microhardness of the glass-ceramic compared to the parental glass; both lie in the upper part of the literature values for abrasion-resistant ceramic tiles used by the building industry. Optimizing the leachability in the glass-ceramic may require adjusting the concentration of calcium to reduce the crystallization of akermanite, promoting the formation of more spinel-like phases and pyroxene. The designed process proposes a process to use basalt as an inertization matrix for sewage sludge transforming them into a product with potential industrial interest.

ACKNOWLEDGMENTS

This research was supported by Consolidated Group for Structure and Materials Desing, 2017SGR1687 and by the Fundació Bosch i Gimpera Project 307466. The authors would like to thank the staff of the Centres Científics i

Tecnològics of the University of Barcelona (CCiTUB) for their technical support, Esther Vilalta and the Departament de Ciència de Materials i Enginyeria Metal·lúrgica for the access to the Vickers microindenter. The manuscript was improved thanks to the comments of two anonymous reviewers. M. Tarragó received support from a PhD grant from the Ministerio de Educación, Cultura y Deporte (FPU13/04507).

ORCID

Mariona Tarrago https://orcid.org/0000-0002-0325-6955
Daniel R. Neuville https://orcid.org/0000-0002-8487-5001

REFERENCES

1. EPA. Land Application of Sewage Sludge. Fed Regist. 1994.
2. Zhang Q, Hu J, Lee DJ, Chang Y, Lee YJ. Sludge treatment: current research trends. Bioresour Technol. 2017;243:1159–72.
3. Agència Catalana de l'Aigua. Gestió de Biosòlids a Catalunya. 2018.
4. Inglezakis VJ, Zorpas AA, Karagiannidis A, Samaras P, Voukkali I, Sklari S. European Union Legislation on Sewage Sludge Management. 2016;23(2):635–9.
5. Tytła M. Assessment of heavy metal pollution and potential ecological risk in sewage sludge from municipal wastewater treatment plant located in the most industrialized region in poland—case study. Int J Environ Res Public Health. 2019;16(13):1–16.
6. Guillemet TA, Maesen P, Delcarte E, Lognay GC, Gillet A, Claustriaux JJ, et al. Factors influencing microbiological and chemical composition of South-Belgian raw sludge. Biotechnol Agron Soc Environ. 2009;13(2):249–55.
7. Ansari MI, Malik A. Seasonal variation of different microorganisms with nickel and cadmium in the industrial wastewater and agricultural soils. Environ Monit Assess. 2010;167(1–4):151–63.
8. Hecht NL, Duvall DS. Characterization and Utilization of municipal and utility sludges and ashes. 1975.
9. Tarragó M. Modelization of the vitrification of sewage sludge using a basaltic matrix. Doctoral thesis, Universitat de Barcelona. 2018.
10. Romero M, Rincón JM. Microstructural characterization of a goethite waste from zinc hydrometallurgical process. Mater Lett. 1997;31(1–2):67–73.
11. Bingham PA, Hand RJ. Vitrification of toxic wastes: a brief review. Adv Appl Ceram. 2006;105(1):21–31.
12. Hossain MK, Strezov V, Nelson PF. Thermal characterisation of the products of wastewater sludge pyrolysis. J Anal Appl Pyrolysis. 2009;85(1–2):442–6.
13. Bernardo E, Dal Maschio R. Glass-ceramics from vitrified sewage sludge pyrolysis residues and recycled glasses. Waste Manag. 2011;31(11):2245–52.
14. Ischia M, Maschio RD, Grigiante M, Baratieri M. Clay-sewage sludge co-pyrolysis. A TG-MS and Py-GC study on potential advantages afforded by the presence of clay in the pyrolysis of wastewater sewage sludge. Waste Manag. 2011;31(1):71–7.
15. Lin DF, Chang WC, Yuan C, Luo HL. Production and characterization of glazed tiles containing incinerated sewage sludge. Waste Manag. 2008;28(3):502–8.
16. Tian Y, Zuo W, Chen D. Crystallization evolution, microstructure and properties of sewage sludge-based glass-ceramics prepared by microwave heating. J Hazard Mater. 2011;196:370–9.
17. Sánchez ME, Menéndez JA, Domínguez A, Pis JJ, Martínez O, Calvo LF, et al. Effect of pyrolysis temperature on the composition of the oils obtained from sewage sludge. Biomass Bioenerg. 2009;33(6–7):933–40.
18. Font R, Fullana A, Conesa JA, Llavador F. Analysis of the pyrolysis and combustion of different sewage sludges by TG. J Anal Appl Pyrolysis. 2001;58–59:927–41.
19. Pokorna E, Postelmans N, Jenicek P, Schreurs S, Carleer R, Yperman J. Study of bio-oils and solids from flash pyrolysis of sewage sludges. Fuel. 2009;88(8):1344–50.
20. Fonts I, Gea G, Azuara M, Ábrego J, Arauzo J. Sewage sludge pyrolysis for liquid production: a review. Renew Sustain Energy Rev. 2012;16(5):2781–805.
21. Gong M, Zhu W, Xu ZR, Zhang HW, Yang HP. Influence of sludge properties on the direct gasification of dewatered sewage sludge in supercritical water. Renew Energy. 2014;66:605–11.
22. Cao JP, Shi P, Zhao XY, Wei XY, Takarada T. Catalytic reforming of volatiles and nitrogen compounds from sewage sludge pyrolysis to clean hydrogen and synthetic gas over a nickel catalyst. Fuel Process Technol. 2014;123:34–40.
23. Tervahauta T, Rani S, Hernández Leal L, Buisman CJNN, Zeeman G. Black water sludge reuse in agriculture: Are heavy metals a problem? J Hazard Mater. 2014;274:229–36.
24. Montero MAA, Jordán MMM, Hernández-Crespo MSS, Sanfeliu T. The use of sewage sludge and marble residues in the manufacture of ceramic tile bodies. Appl Clay Sci. 2009;46:404–8.
25. Pavšič P, Mladenovič A, Mauko A, Kramar S, Dolenec M, Vončina E, et al. Sewage sludge/biomass ash based products for sustainable construction. J Clean Prod. 2014;67:117–24.
26. Zhou J, Li T, Zhang Q, Wang Y, Shu Z. Direct-utilization of sewage sludge to prepare split tiles. Ceram Int. 2013;39(8):9179–86.
27. Dominguez A, Menendez JA, Inguanzo M, Pis JJ. Production of bio-fuels by high temperature pyrolysis of sewage sludge using conventional and microwave heating. Bioresour Technol. 2006;97(10):1185–93.
28. Menéndez JA, Domínguez A, Inguanzo M, Pis JJ. Microwave-induced drying, pyrolysis and gasification (MWDPG) of sewage sludge: vitrification of the solid residue. J Anal Appl Pyrolysis. 2005;74(1–2):406–12.
29. Domínguez A, Fernández Y, Fidalgo B, Pis JJ, Menéndez JA. Biosyngas production with low concentrations of CO2and CH4 from microwave-induced pyrolysis of wet and dried sewage sludge. Chemosphere. 2008;70(3):397–403.
30. Kikuchi R. Vitrification process for treatment of sewage sludge and incineration ash. J Air Waste Manag Assoc. 1998;48(11):1112–5.
31. Ferreiro-Domínguez N, Rigueiro-Rodríguez A, Bianchetto E, Mosquera-Losada MR. Effect of lime and sewage sludge fertilisation on tree and understory interaction in a silvopastoral system. Agric Ecosyst Environ. 2014;188:72–9.
32. Singh RP, Agrawal M. Potential benefits and risks of land application of sewage sludge. Waste Manag. 2008;28(2):347–58.
33. Forsberg LS, Ledin S. Effects of sewage sludge on pH and plant availability of metals in oxidising sulphide mine tailings. Sci Total Environ. 2006;358(1–3):21–35.
34. Rawlings RD, Wu JP, Boccaccini AR. Glass-ceramics: their production from wastes-A Review. J Mater Sci. 2006;41(3):733–61.
35. Monteiro SN, Alexandre J, Margem JI, Sánchez R, Vieira CMF. Incorporation of sludge waste from water treatment plant into red ceramic. Constr Build Mater. 2008;22(6):1281–7.

36. Majima T, Tadao K, Naruse M, Hiraoka M. Studies on Pyrolysis Process of Sewage Sludge. International Association on Water Pollution Research; 1978. https://doi.org/10.1016/B978U0U08U020902U9.50052U3
37. Celis J, Sandoval M, Barra R. Plant response to salmon wastes and sewage sludge used as organic fertilizer on two degraded soils under greenhouse conditions. Chil J Agric Res. 2008;68(3):274–84.
38. Roig N, Sierra J, Martí E, Nadal M, Schuhmacher M, Domingo JL. Long-term amendment of Spanish soils with sewage sludge: effects on soil functioning. Agric Ecosyst Environ. 2012;158:41–8.
39. Borowski G. Application of vitrification method for the disposal of municipal sewage sludge. 2013.
40. Folgueras MB, Díaz RM, Xiberta J, Prieto I. Thermogravimetric analysis of the co-combustion of coal and sewage sludge. Fuel. 2003;82(15–17):2051–5.
41. Metcalf E. Wastewater engineering - treatment, disposal and reuse, 3rd edn. New York, USA: McGraw Hill; 1991.
42. Suzuki S, Tanaka M, Kaneko T. Glass-ceramic from sewage sludge ash. J Mater Sci. 1997;2:1775–9.
43. Erol M, Küçükbayrak S, Ersoy-Meriçboyu A. Production of glass-ceramics obtained from industrial wastes by means of controlled nucleation and crystallization. Chem Eng J. 2007;132(1–3):335–43.
44. Do YS, Yun YH. Preparation of glass ceramics from sludge bottom ash and waste glass. J Ceram Process Res. 2011;12(4):361–4.
45. Juoi JM, Arudra D, Rosli ZM, Hussain K, Japper Jaafar A. Microstructural properties of glass composite material made from incinerated scheduled waste slag and soda lime silicate (SLS) waste glass. J Non Cryst Solids. 2013;367(1):8–13.
46. Barbieri L, Corradi Bonamartini A, Lancellotti I. Alkaline and alkaline-earth silicate glasses and glass-ceramics from municipal and industrial wastes. J Eur Ceram Soc. 2000;20(14–15):2477–83.
47. Park YJ, Moon SO, Heo J. Crystalline phase control of glass ceramics obtained from sewage sludge fly ash. Ceram Int. 2003;29(2):223–7.
48. O'Neill HSC, Jenner FE. The global pattern of trace-element distributions in ocean floor basalts. Nature. 2012;491(7426):698–704.
49. Dasgupta R, Jackson MG, Lee CTA. Major element chemistry of ocean island basalts - conditions of mantle melting and heterogeneity of mantle source. Earth Planet Sci Lett. 2010;289(3–4):377–92.
50. Haug RT, Kuchenrither R, Oerke D, Soszynski S, Zenz D. Sludge processing technology. InLue-Hing C, et al., Munic. Sew. Sludge Manag. Process. Util. Dispos. 1992:223–98.
51. Allievi L, Colombi A, Calcaterra E, Ferrari A. Inactivation of fecal bacteria in sewage sludge by alkaline treatment. Bioresour Technol. 1994;49(1):25–30.
52. Tarrago M, Garcia-Valles M, Martínez S, Neuville DR. Phosphorus solubility in basaltic glass: limitations for phosphorus immobilization in glass and glass-ceramics. J Environ Manage. 2018;220:54–64.
53. Garcia-Valles M, Avila G, Martinez S, Terradas R, Nogues JM. Heavy metal-rich wastes sequester in mineral phases through a glass-ceramic process. Chemosphere. 2007;68(10):1946–53.
54. Tarrago M, Garcia-Valles M, Aly MHH, Martinez S. Valorization of sludge from a wastewater treatment plant by glass-ceramic production. Ceram Int. 2017;43(1):930–7.
55. Holand W, Beall GH. Glass-ceramic Technology. 2012. https://doi.org/10.1002/9781118265987.fmatter
56. Vitrokeramik PN. Grundlagen der Technologie. 1986.
57. Agarwal G, Speyer RF. Devitrification hardening of cupola slag glass with CaO and SiO_2 additions. J Non Cryst Solids. 1991;135(2–3):95–104.
58. Fredericci C, Zanotto ED, Ziemath ECC. Crystallization mechanism and properties of a blast furnace slag glass. J Non Cryst Solids. 2000;273:64–75.
59. Arancibia JRHH, Alfonso P, García-Valles M, Martínez S, Parcerisa D, Canet C, et al. Obtención de vidrio a partir de residuos de la minería del estaño en Bolivia. Bol la Soc Esp Ceram y Vidr. 2013;52(3):143–50.
60. Shi J, Feng H, Ye C, Hu L, Xie J, Yang H, et al. Preparation and characterization of $CaO{\cdot}Al_2O_3{\cdot}SiO_2$ glass-ceramics from molybdenum tailings. Mater Chem Phys. 2017;197:57–64.
61. Alfonso P, Castro D, Garcia-Valles M, Tarrago M, Tomasa O, Martinez S. Recycling of tailings from the Barruecopardo tungsten deposit for the production of glass. J Therm Anal Calorim. 2016;125(2):681–7.
62. Alfonso P, Tomasa O, Garcia-Valles M, Tarrago M, Martínez S, Esteves H. Potential of tungsten tailings as glass raw materials. Mater Lett. 2018;228:456–8.
63. Araña V, Aparicio A, Escorza CM, Cacho LG, Ortiz R, Vaquer R, et al. El volcanismo neógeno-cuaternario de Catalunya: caracteres estructurales, petrológicos y geodinámicos. Acta Geol Hisp. 1983;18(1):1–17.
64. Guérin G, Benhamou G, Mallarach J-M. Un exemple de fusió parcial en medi continental: el vulcanisme quaternari de Catalunya. Vitrina. 1986;1985(1):20–6.
65. Le Losq C, Neuville DR, Moretti R, Roux J. Determination of water content in silicate glasses using Raman spectrometry: implications for the study of explosive volcanism. Am Mineral. 2012;97(5–6):779–90.
66. CRC. Handbook of Chemistry and Physics, Internet Version. Boca Raton, FL: CRC Press; 2005.
67. Le Losq C, Neuville DR, Florian P, Henderson GS, Massiot D. The role of Al3+ on rheology and structural changes in sodium silicate and aluminosilicate glasses and melts. Geochim Cosmochim Acta. 2014;126:495–517.
68. Marotta A, Buri A, Branda F. Nucleation in glass and differential thermal analysis. J Mater Sci. 1981;16(2):341–4.
69. Monshi A, Foroughi MR, Monshi MR. Modified scherrer equation to estimate more accurately nano-crystallite size using XRD. World J Nano Sci Eng. 2012;02(03):154–60.
70. Rodríguez-Carvajal J. Recent advances in magnetic structure determination by neutron powder diffraction. Phys B Condens Matter. 1993;192:55–69.
71. Garcia-Valles M, Hafez HS, Cruz-Matias I, Verges E, Aly MH, Nogues J, et al. Calculation of viscosity-temperature curves for glass obtained from four wastewater treatment plants in Egypt. J Therm Anal Calorim. 2013;111(1):107–14.
72. Pascual MJ, Pascual L, Duran A. Determination of the viscosity-temperature curve for glasses on the basis of the fixed viscosity points determined by hot stage microscopy. Phys Chem Glas. 2001;42(1):61–6.
73. Kress VC, Carmichael ISE. Stoichiometry of the iron oxidation reaction in silicate melts. Am Mineral. 1988;73:1267–74.
74. DIN-38414S4. Deutsche Einheitsverfahren zur Wasser, Abwasserund Schlammuntersuchung, Bestimmung der Eluierbarkeit von Wasser (S4). 1984.
75. McMillan PF, Piriou B. The structures and vibrational spectra of crystals and glasses in the silica-alumina system. J Non Cryst Solids. 1982;53(3):279–98.
76. Mysen BO, Virgo D, Scarfe CM. Relations between anionic structure and viscosity of silicate melts - A Raman spectroscopic study. Am Mineral. 1980;65:690–710.

77. Neuville DR. Viscosity, structure and mixing in (Ca, Na) silicate melts. Chem Geol. 2006;229(1–3):28–41.
78. Neuville DR, de Ligny D, Henderson GS. Advances in Raman Spectroscopy applied to earth and material sciences. Rev Mineral Geochemistry. 2014;78(1):509–41.
79. Neuville DR, Mysen BO. Role of aluminium in the silicate network: In situ, high-temperature study of glasses and melts on the join SiO_2-$NaAlO_2$. Geochim Cosmochim Acta. 1996;60(10):1727–37.
80. Pasquarello A, Sarnthein J, Car R. Dynamic structure factor of vitreous silica from first principles: comparison to neutron-inelastic-scattering experiments. Phys Rev B - Condens Matter Mater Phys. 1998;57(22):14133–40.
81. Seifert FA, Mysen BO, Virgo D. Three-dimensional network structure of quenched melts (glass) in the systems SiO_2-$NaAlO_2$, SiO_2-$CaAl_2O_4$and SiO_2-$MgAl_2O_4$. Am Mineral. 1982;67(7–8):696–717.
82. Umari P, Gonze X, Pasquarello A. Concentration of small ring structures in vitreous silica from a first-principles analysis of the Raman Spectrum. Phys Rev Lett. 2003;90(2):4.
83. Hehlen B, Neuville DR. Raman response of network modifier cations in alumino-silicate glasses. J Phys Chem B. 2015;119(10):4093–8.
84. Matson DW, Sharma SK, Philpotts JA. The structure of high-silica alkali-silicate glasses. A Raman spectroscopic investigation. J Non Cryst Solids. 1983;58(2–3):323–52.
85. McMillan PF. Structural studies of silicate glasses and melts-applications and limitations of Raman Spectroscopy. Am Mineral. 1984;69:622–44.
86. Le Losq C, Neuville DR. Effect of the Na/K mixing on the structure and the rheology of tectosilicate silica-rich melts. Chem Geol. 2013;346:57–71.
87. Bell RJ, Dean P. Localization of phonons in vitreous silica and related glasses. Int Conf Phys Non-Crystalline Solids. 1972;22:375–82.
88. Furukawa T, Fox KE, White WB. Raman spectroscopic investigation of the structure of silicate glasses. III. Raman intensities and structural units in sodium silicate glasses. J Chem Phys. 1981;75(7):3226–37.
89. Mysen BO, Toplis MJ. Structural behavior of Al3+ in peralkaline, metaluminous, and peraluminous silicate melts and glasses at ambient pressure. Am Mineral. 2007;92(5–6):933–46.
90. Cochain B, Neuville DR, Henderson GSS, McCammon CAA, Pinet O, Richet P. Effects of the iron content and redox state on the structure of sodium borosilicate glasses: a Raman, Mössbauer and boron k-edge xanes spectroscopy study. J Am Ceram Soc. 2012;95(3):962–71.
91. Magnien V, Neuville DR, Cormier L, Roux J, Hazemann JL, Pinet O, et al. Kinetics of iron redox reactions in silicate liquids: a high-temperature X-ray absorption and Raman spectroscopy study. J Nucl Mater. 2006;352(1–3):190–5.
92. Virgo D, Mysen BO. The structural state of iron in oxidized vs. reduced glasses at 1 atm: A57Fe Mössbauer study. Phys Chem Miner. 1985;12(2):65–76.
93. Magnien V, Neuville DR, Cormier L, Roux J, Hazemann JL, de Ligny D, et al. Kinetics and mechanisms of iron redox reactions in silicate melts: the effects of temperature and alkali cations. Geochim Cosmochim Acta. 2008;72(8):2157–68.
94. Magnien V, Neuville DR, Cormier L, Mysen BO, Briois V, Belin S, et al. Kinetics of iron oxidation in silicate melts: a preliminary XANES study. Chem Geol. 2004;213(1–3):253–63.
95. Moretti R. Polymerisation, basicity, oxidation state and their role in ionic modelling of silicate melts. Ann Geophys. 2005;48(4–5):583–608.
96. Morse SA. Basalts and phase diagrams: An introduction to the quantitative use of phase diagrams in igneous petrology. New York: Springer; 1980; 1–493.
97. Levin EM, McMurdie HF. Phase diagrams for ceramists 1975 Supplement. Am Ceram Soc. 1975.
98. Villeneuve N, Neuville DR, Boivin P, Bachèlery P, Richet P. Magma crystallization and viscosity: a study of molten basalts from the Piton de la Fournaise volcano (La Réunion island). Chem Geol. 2008;256(3–4):241–50.
99. Tarragó M, Esteves H, Garcia-Valles M, Martínez S, Neuville DR, Tarrago M, et al. Effect of Ca in P-doped basaltic glass-ceramics: application to waste inertization. Mater Lett. 2018;220:266–8.
100. Kuzmin KL, Zhukovskaya ES, Gutnikov SI, Pavlov YV, Lazoryak BI. Effects of ion exchange on the mechanical properties of basaltic glass fibers. Int J Appl Glas Sci. 2016;7(1):118–27.
101. Sasaki S. Radial distribution of electron density in magnetite, Fe_3O_4. Acta Crystallogr Sect B Struct Sci. 1997;53:762.
102. Foreman N, Peacor DRN. Refinement of the nepheline structure at several temperatures. Zeitschrift für Krist. 1970;132(1–6):45–70.
103. Peacor DN. Refinement of the crystal structure of a pyroxene of formula M_{II} M_{III} $(Si_{1.5}Al_{0.5})O_{61}$. Am Mineral. 1967;52:31–41.
104. Yamaguchi G, Suzuki K. Structural analysis of merwinite. J Ceram Assoc Japan. 1967;75(863):220–9.
105. Swainson IP, Dove MT, Schmahl WW, Putnis A. Neutron powder diffraction study of the åkermanite-gehlenite solid solution series. Phys Chem Miner. 1992;19(3):185–95.
106. Orsini PG, Buri A, Marotta A. Devitrification of glasses in the Akermanite-Gehlenite system. J Am Ceram Soc. 1974;58(7):306–11.
107. Beall GH, Rittler HL. Basalt glass ceramics. Am Ceram Soc Bull. 1976;55(6):579–82.
108. Alfonso P. Mineralogía y aptitudes vitrocerámicas de materiales magmáticos neógenos de Cataluña. 1985.
109. De Vicente Mingarro I. Estudio de los mecanismos de nucleación y cristalización en vidrios obtenidos a partir de rocas basálticas canarias. Doctoral theses, 1992.
110. Jensen M, Smedskjaer MM, Estrup M, Kristjansson M, Lönnroth N, Yue YZ. Hardness of basaltic glass-ceramics. Glas Technol Eur J Glas Sci Technol Part A. 2009;50(4):189–95.
111. El-Shennawi AWA, Mandour MA, Morsi MM, Abdel-Hameed SAM. Monopyroxenic basalt-based glass-ceramics. J Am Ceram Soc. 1999;1999(82):1181–6.
112. McMillan PF, Piriou B. Glass Ceramics. Academic Press; 1975.

How to cite this article: Tarrago M, Royo I, Martínez S, Garcia-Valles M, Neuville DR. Incorporation of calcium in glasses: A key to understand the vitrification of sewage sludge. *Int J Appl Glass Sci*. 2021;12:367–380. https://doi.org/10.1111/ijag.15920